



AIAA 99-0227

**Aerothermodynamic Analysis of Stardust
Sample Return Capsule With Coupled Radiation
and Ablation**

R. N. Gupta
NASA Langley Research Center
Hampton, VA 23681-0001

**37th Aerospace Sciences Meeting
January 11-14, 1999 Reno, NV**

Aerothermodynamic Analysis of Stardust Sample Return Capsule with Coupled Radiation and Ablation

Roop N. Gupta*
NASA Langley Research Center
Hampton, VA 23681

Abstract

An aerothermodynamic analysis of the forebody aeroshell of the Stardust Sample Return Capsule is carried out using the axisymmetric viscous shock-layer (VSL) equations with and without fully coupled radiation and ablation. Formulation of the VSL equations with shoulder radius as the length scale and implementation of the Vigneron pressure condition allow resolution of the flowfield over the shoulder. With a predominantly supersonic outflow over the shoulder, a globally iterated solution of VSL equations can be obtained. The stagnation-point results are obtained along a specified trajectory, whereas detailed calculations along the body are provided at the peak heating point. The coupled laminar and turbulent flow solutions with radiation and ablation are obtained using the equilibrium flow chemistry, whereas a nonequilibrium chemistry model is used for solutions without ablation and turbulence. The equilibrium calculations are physically consistent and a practical way to conserve surface (and flow-field) elemental composition for the current small ablation injection rates, where the surface elemental composition is a mixture of freestream and ablator elements. A maximum stagnation heating of about 1100 W/cm^2 is obtained for the no ablation injection case with nonequilibrium flow chemistry and an equilibrium catalytic wall boundary condition. The corresponding radiative equilibrium wall temperature is about 3800 K . A similar stagnation heating value is obtained with equilibrium flow chemistry. With ablation injection, this value is reduced by about 35%. Reduction in heating due to ablation is slightly less downstream of the stagnation point, along the

conical flank, and over the shoulder. For the ablation injection and turbulent flow solutions, with instantaneous transition just downstream of the stagnation line, the heating is reduced by only about 13% on the conical flank and shoulder from a non-ablating laminar solution. The reduction in heating by ablation injection appears to be partially offset by augmentation due to turbulence in this case.

Nomenclature

C_i	= mass fraction of species I
\tilde{C}_k	= mass fraction of element k
C_P	= frozen specific heat of mixture, J/kg-K
D_{ij}	= binary diffusion coefficient, m^2/s
h_a	= enthalpy of undecomposed ablation material, J/kg
\bar{h}_i	= enthalpy of species i , h_i/V_∞^2
K	= thermal conductivity of mixture, W/m-K
Le	= Lewis number, $\rho D_{ij} C_P/K$
\dot{m}	= mass injection rate, $\text{kg/m}^2\text{-s}$
n_{sh}	= shock standoff distance, m
\bar{n}	= coordinate measured normal to the body, n/R_{C1}
p	= pressure, N/m^2
Pr	= Prandtl number, $\mu C_P/K$
q_c	= $q_{cond} + q_{conv} + q_{diff}$, W/m^2
q_r	= net radiative heat flux in n -direction, $q_r^{(+)} - q_r^{(-)}$, W/m^2

*Senior Research Engineer, Aero-and Gas-Dynamics Division, Associate Fellow, AIAA.

Copyright © 1999 by the American Institute of Aeronautics and Astronautics, Inc. No copyright is asserted in the United States under Title 17, U.S. Code. The U.S. Government has a royalty free license to exercise all rights under the copyright claimed herein for governmental purposes. All other rights are reserved by the copyright owner.

$q_r^{(+)}$	= component of radiative flux toward the shock, W/m ²
$q_r^{(-)}$	= component of radiative flux toward the wall, W/m ²
q_{Total}	= $q_c + q_r$, W/m ²
R_N	= nose radius, m
R_{CI}	= shoulder radius, m
s	= coordinate measured along the surface, m
T	= temperature, K
T_{REWT}	= radiative equilibrium wall temperature, K
T_{ref}	= reference temperature, $V_\infty^2 / C_{p,\infty}$, K
T_{sub}	= sublimation temperature, K
V_∞	= freestream velocity, m/s
$\alpha_{1,j}, \alpha_{2,j}, \alpha_{3,j}$	= curve-fit coefficients for sublimation temperature, T_{sub}
$\beta_{1,j}, \beta_{2,j}, \beta_{3,j}$	= curve-fit coefficients for heat of ablation, ΔH_a
ΔH_a	= heat of ablation, MJ/kg
$\bar{\epsilon}$	= Reynolds number, parameter, $(\mu_{ref} / \rho_\infty V_\infty R_{CI})^{1/2}$
ϵ	= char emissivity, 0.9
$\bar{\mu}$	= viscosity of mixture, μ / μ_{ref}
μ_{ref}	= reference viscosity, $\mu(T_{ref})$, N-s/m ²
ρ	= density of mixture, kg/m ³
σ	= Stefan-Boltzmann constant, 5.668×10^{-8} W/(m ² -K ⁴)

Subscripts

A	= ablator
$cond$	= conduction
$conv$	= convection
$diff$	= diffusion

Eq	= equilibrium
i	= i^{th} species
j	= j^{th} species
k	= k^{th} element
r	= radiation
w	= wall value
-	= values for the solid ablation material at the surface
∞	= freestream value

Superscripts

-	= nondimensional quantity
---	---------------------------

Introduction

The STARDUST mission¹, part of NASA's Discovery Program, plans to fly a spacecraft through the tail of the comet Wild-2 and bring samples of cometary material as well as interstellar dust to Earth for analysis. The collected cometary particles and the dust will be contained in the Stardust Sample Return Capsule (SRC) which must survive an intense Earth entry heating. At 12.6 km/s, the SRC entry is the fastest ever attempted into the Earth's atmosphere. This paper focuses on the aerothermodynamic issues concerning the flow environment around the SRC forebody during such an entry.

Since STARDUST is scheduled for launch in early 1999, the work presented here was not available in time to impact the SRC design. However, a better understanding of the SRC entry environment and the computational tools employed for its analysis will help in promoting a better and more efficient design of the thermal protection system (TPS) for future sample return vehicles such as MUSES-C, Genesis, Champollion (DS-4), and Mars Sample Return. Improved computational tools will also be useful in post-flight evaluation of the TPS and other measured quantities.

Recent entry flowfield results² have been obtained to size the Stardust SRC forebody TPS. These calculations are made with an axisymmetric Navier-Stokes flow solver, loosely coupled to the radiation and ablation modules. The flowfield calculations with ablation are based on an 18-species chemical model under thermochemical

nonequilibrium condition. The ablation boundary condition (namely, the blowing rate, species mass fractions, and wall temperature) for the flowfield solution are obtained iteratively by assuming the surface composition to be in equilibrium at the temperatures and pressures predicted from a material response code (with inputs of wall heat transfer rate and pressure from the flowfield solution). However, the elemental conservation equations are not solved to obtain a continuous elemental transition³ in the flowfield even though the elemental compositions of the freestream and ablator surface are different. Non-enforcement of elemental conservation in this case may result in a non-unique solution. Further, if an equilibrium surface boundary condition is employed with a nonequilibrium flowfield solver, then care should be taken to use a consistent set of chemical species for both the equilibrium and nonequilibrium solvers.

When the flowfield analysis is based on a nonequilibrium flow model and the surface composition is specified by the equilibrium assumption, an important question arises as to what method is used to establish the elemental composition at the surface with both ablation and freestream elements present. For an accurate definition of the surface elemental composition (i.e., elemental surface boundary condition), a methodology must be used that implements the inherent surface and flowfield elemental coupling. For the case when both the flowfield and surface ablation species are calculated using the equilibrium assumption, one can solve the elemental continuity equations (iteratively) for each element to determine the appropriate mix of ablative and freestream elemental composition at the surface (adjacent to the ablator) and through the flowfield. With information concerning the elemental composition, pressure, and temperature, one can then calculate species concentration at the surface (adjacent to the ablator) and through the flowfield using free energy minimization or other procedures. Thus, with the calculation of both the flowfield and surface ablation species from the equilibrium assumption, the transition from ablation to freestream elements (and the corresponding species) is obtained continuously through the solution of elemental continuity equations, and also the transition from equilibrium to nonequilibrium does not occur instantaneously right next to an ablating surface. Further, the fully equilibrium calculations also bypass the entire discussion about governing processes and intermediate steps concerning the number of species, reaction mecha-

nisms, and the associated reaction rates, especially for the complex flowfields with ablation. Since the primary focus in the design of TPS is on surface quantities (such as temperature, pressure, heat transfer, shear, integrated heat load etc.), flowfield calculations with the thermochemical equilibrium model would appear adequate (for the convective dominated heating environment), especially, if the ablation boundary condition is specified with the equilibrium assumption.

Employing a methodology similar to that of Ref. 2, Ref. 4 recently obtained stagnation-point heat transfer rates for the Pioneer-Venus probes⁵, whose flight environment resembles that of current sample return vehicles^{2,6}. A 17-species nonequilibrium chemistry model is used for the shock-layer flow. The pyrolysis gas composition at the surface is obtained by assuming that the surface is in equilibrium at the local temperature and pressure. It is not obvious from Ref. 4, however, how some of the pyrolysis species such as CH_2 , CH_3 , CH_4 , C_3 , etc. (which do not appear in the shock layer chemistry model of Ref. 7 used in Ref. 4) are accounted for in the boundary condition specification for the shock-layer species continuity equations. Once again, in absence of a method to establish the elemental composition at the surface and through the shock layer with the presence of both ablation and freestream species, there appears to be a mismatch between the surface and shock-layer species, and a smooth transition of the elemental composition from surface to freestream value is not implemented.

A recent analysis⁸ of the MUSES-C asteroid sample return mission considered a 19-species nonequilibrium chemistry model (with the thermal equilibrium assumption) both for the shock-layer flow and the ablator surface for a true ablation calculation. The chemistry model consists of 11 air species and 8 carbon-containing species. The hydrocarbon species are not included and the pyrolysis process is not considered to keep the analysis simple. Since the 19-species finite-rate chemistry model is implemented both at the surface and in the shock-layer, it includes all the species considered throughout the computational domain. Thus, the analysis is consistent and the elemental composition is conserved both at the surface and through the shock layer for the chemistry model considered and the case where the species present at the surface are only ablator species. The problem, however, arises when the freestream species are also present at the surface along with the ablator species. Similar to Refs. 2

and 4, no method is provided to establish the surface elemental composition (and hence the species boundary condition) for such a situation, which is usually the case before large scale oxidation and ablation drive the freestream species away from the surface.

Thus, it becomes essential to compare the finite-rate flowfield chemistry solutions with equilibrium as well as nonequilibrium surface ablation with those obtained with the assumption of full chemical equilibrium both at the surface and in the shock-layer. Apart from the simplicity of the physics, a full equilibrium calculation also provides a conservative estimate of the surface heating.

Further, for a nonablating surface, using a fully catalytic wall boundary condition² (with complete recombination to freestream value) may not be realistic at temperatures greater than 2000 K. A physically consistent boundary condition in this case would be an equilibrium catalytic wall, which would reduce to a fully catalytic boundary condition at lower temperatures (i.e. <2000 K).

In the present work, the Stardust SRC entry flowfield is investigated by assuming complete thermal equilibrium. Fully coupled radiation solutions with and without ablation injection are obtained using an axisymmetric viscous shock-layer (VSL) method by assuming chemical equilibrium both in the flowfield and at the surface. Computed results include those with the laminar flow assumption as well as those for a fully turbulent flow immediately downstream of the stagnation line. To evaluate the effect of using a fully catalytic wall boundary condition (for a nonablating surface) on surface heating and temperature, results have also been obtained from the VSL method with nonequilibrium chemistry and different wall boundary conditions.

Analysis

Flowfield Model

The VSL equations employed are those of a multicomponent reacting gas mixture under conditions of chemical nonequilibrium⁹ and equilibrium^{10,11} with thermal equilibrium. These equations are the same as those given in Refs. 9-11 and, therefore, they are not given here. The chemistry model, boundary conditions, and

thermodynamic and transport properties employed are similar to those of Refs. 9-12, whereas the ablation injection, radiative transport, and turbulence models (used with equilibrium chemistry only) are those of Refs. 10-14. These are briefly described here.

Chemistry Model. For calculations of air flow over a non-ablating surface, an 11-species (N_2 , O_2 , N , O , NO , NO^+ , e^- , N^+ , O^+ , N_2^+ , and O_2^+) chemistry model is used for nonequilibrium calculations whereas a 9-species (N_2 , O_2 , N , O , NO , NO^+ , e^- , N^+ , and O^+) chemical model is used for the equilibrium flow. For the equilibrium ablation injection calculation, 20 chemical species are used: the seven equilibrium air species (without NO and NO^+) plus C , C_2 , C_3 , CO , CN , C_2H , C_3H , C_4H , C_2H_2 , C^+ , H , H_2 , and HCN . The equilibrium composition is determined (for a given temperature, pressure, and elemental composition) by using the free-energy minimization method of Ref. 15.

Boundary Conditions. The boundary conditions at the shock are obtained by using the Rankine-Hugoniot relations. The flow behind the shock is assumed to be in chemical equilibrium or frozen at the freestream composition for equilibrium and nonequilibrium calculations, respectively⁹. No-slip continuum boundary conditions are employed at the surface. The surface temperature with no ablation injection is assumed to be the radiative equilibrium wall value obtained from

$$T_{REWT} = \left\{ \left[\bar{q}_r^{(-)} + \bar{\epsilon}^2 \left(\bar{K} \frac{\partial \bar{T}}{\partial \bar{n}} + \bar{\mu} \frac{Le}{Pr} \sum_{i=1}^{N_s} \bar{h}_i \frac{\partial C_i}{\partial \bar{n}} \right) \right] \times \frac{\rho_\infty V_\infty^3}{\epsilon \sigma} \right\}^{1/4} \quad (1)$$

For ablation injection cases, steady state ablation is assumed. However, the species surface concentrations, ablation rates, and surface temperatures, in general, can be obtained from a material response code (such as FIAT of Ref. 2), by employing input surface heat flux and pressure from an equilibrium flowfield code. For the surface ablation cases considered in the present study, an energy balance at the

flowfield-ablator interface gives the coupled mass injection rate for quasi-steady ablation:

$$\dot{m} = \left(\frac{-q_{c,w} - q_{r,w}}{\sum_{i=1}^{N_s} (C_i h_i)_w - h_a} \right) \quad (2)$$

The surface temperature for the present calculations with ablation injection is that at which the quasi-steady ablation occurs. The expression used for surface temperature for the Phenolic Impregnated Ceramic Ablator (PICA)¹⁶ has been obtained by curve-fitting these values (computed from the charring material and ablation (CMA) thermal^{17,18} response code) in the pressure range $0.001 \text{ atm} < p < 1.00 \text{ atm}$. The elemental composition of PICA is similar to that of a carbon-phenolic ablator. It is, however, less dense and has much lower thermal conductivity. The expressions for the sublimation temperature and heat of ablation for PICA (with 92% carbon, 4.9% oxygen, 2.2% hydrogen, and 0.9% nitrogen by mass) are:

$$T_{abl} = \sum_{j=1}^5 \alpha_{1,j} (\log C_A)^{j-1} + (\log p_w) \sum_{j=1}^5 \alpha_{2,j} \\ \times (\log C_A)^{j-1} + (\log p_w)^2 \sum_{j=1}^5 \alpha_{3,j} (\log C_A)^{j-1} \quad (3)$$

where p_w is the wall pressure in atmosphere and C_A is the ablator mass fraction at the surface. The values for $\alpha_{i,j}$ are given in Table 1. For the case, when the gas species adjacent to the surface are due solely to the ablation species (i.e. $C_A = 1.0$), Eq. (3) with the values of $\alpha_{i,j}$ in Table 1 gives

$$T_{abl} = 3790.0 + 329.94(\log p_w) \\ + 20.386(\log p_w)^2, \text{ K} \quad (4)$$

The surface temperature and the coupled mass injection rate are calculated by iterating the solution of the governing flowfield equations and the boundary conditions.

For ablation injection, the elemental concentrations at the wall are governed by convection and diffusion and are obtained from the equation

$$\left(\frac{\partial \bar{C}_k}{\partial \bar{n}} \right)_w - \frac{1}{\bar{\epsilon}^2} \left(\frac{\dot{m} Pr}{\mu Le} \right)_w \left[(\bar{C}_k)_w - (\bar{C}_k)_- \right] = 0 \quad (5)$$

For the radiative transport calculations, the bow shock is considered transparent and the freestream is considered cold and transparent. Therefore, the precursor effects are neglected. Further, the body surface is assumed to be gray with a reflectivity of 0.1, emissivity of 0.9, and transmissivity of 0. The energy reradiated from the surface is included both in the radiation transport calculation as well in the surface energy balance [Eq. (2)]. The net radiative flux can be represented as

$$q_r = q_r^{(+)} - q_r^{(-)} \quad (6)$$

At the surface,

$$q_{r,w}^{(+)} = \epsilon \sigma T_w^4 \quad (7)$$

The heat transferred to the wall because of conduction, diffusion, and convection is

$$-q_{c,w} = \bar{\epsilon}^2 \rho_\infty V_\infty^3 \left[\bar{K} \frac{\partial \bar{T}}{\partial \bar{n}} + \mu \frac{Le}{Pr} \sum_{i=1}^{NS} \bar{h}_i \frac{\partial C_i}{\partial \bar{n}} \right. \\ \left. - \frac{\dot{m}}{\rho_\infty V_\infty} \sum_{i=1}^{NS} (C_i \bar{h}_i - C_{i-} \bar{h}_{i-})_w \right] \quad (8)$$

where NS is the number of species.

Catalytic Wall Conditions. For nonablating, nonequilibrium flow, three catalytic wall boundary conditions are used:

(i) **Noncatalytic Wall (NCW):** Since no reactions occur at the surface in this case, the mass-fraction gradients for all species are zero at the surface, i.e.,

$$\left(\frac{\partial C_i}{\partial \bar{n}} \right)_w = 0 \quad (9)$$

(ii) Equilibrium Catalytic Wall (ECW): The wall catalyzed reactions are assumed to occur at an infinite rate and, therefore, the species mass fractions at the wall are those corresponding to their local equilibrium values, i.e.,

$$(C_i)_w = (C_i)_{Eq} = f(p_w, T_w) \quad (10)$$

(iii) Fully Catalytic Wall (FCW): The gas species at the surface are assumed to recombine to the freestream composition, i.e.,

$$(C_i)_w = (C_i)_\infty \quad (11)$$

At low surface temperatures, the surface condition of Eq. (10) reduces to Eq. (11).

Radiative Transport. The radiation transport code RADICAL^{19,20} has been used to compute radiative heat flux, q_r . This code accounts for the effects of nongray self-absorption and includes the molecular band, continuum, and atomic line transitions. The ultraviolet properties for C_3 are taken from Ref. 21. The radiative transport is fully coupled with the flowfield solutions for equilibrium chemistry. The nonequilibrium total heat transfer rate (for a nonablating surface) is obtained by adding the equilibrium radiative component to the nonequilibrium conductive and diffusive components.

Thermodynamics and Transport Properties. Thermodynamic properties for specific heat, enthalpy and free energy, and transport properties for viscosity and thermal conductivity are required for each species considered. Values of these properties are obtained by using polynomial curve fits of Refs. 10 and 12. The equilibrium composition is determined by a free-energy minimization calculation procedure of Ref. 15. Mixture viscosity is obtained by the method of Armaly and Sutton²² and mixture thermal conductivity is computed by the Maxon and Saxena²³ relation. The Lewis number is set¹⁰ equal to 1.4.

Turbulence Model. A two-layer eddy-viscosity turbulence model of Cebeci-Smith^{14,24,25} is employed in the present investigation. Reference 25 gives a detailed description of the model and various expressions for it. The boundary-layer edge definition used in the current study is based on an index of diffusion, conduction, and dissipation. The transition to turbulent flow is assumed to occur instantaneously at the first grid point downstream of the stagnation point. The turbulent Prandtl and Lewis numbers are assumed to be 0.9 and 1.0, respectively.

Solution Procedure

The method used to solve the nonequilibrium and equilibrium VSL equations is a spatial-marching, implicit, finite-difference technique^{3,14}, which includes coupling of the global continuity and normal momentum equations and use of the Vigneron pressure condition in the subsonic region (which covers a large part of the forebody of STARDUST capsule shown in Fig. 1). The shoulder radius R_{C1} is employed for the reference length in place of the conventionally used nose radius, R_N . Details of the method of solution are similar to those of Refs. 3 and 14 and, therefore, are not presented here.

Results and Discussion

Results are presented for the forebody of the Stardust Sample Return Capsule (SRC) shown in Fig. 1. The overshoot entry trajectory² (which produces maximum heat loads) used in the calculations is given in Fig. 2. The freestream conditions at the calculation points for this trajectory are provided in Table 2. Peak heating and pressure occur at approximately 54 s and 66 s, respectively, for this trajectory. The SRC forebody is an axisymmetric 60-deg sphere-cone with a nose radius, R_N , of approximately 23 cm. The computational domain for the present VSL results extends to just past the highest point, C1, on the shoulder, where the flow is predominantly supersonic. The PICA heatshield for the forebody extends beyond this point². A 100×125 grid is employed with all the computations. Variable grid sizes are used both normal to and along the body surface. The minimum distance between normal grid points is $2 \times 10^{-4} R_{C1}$. In the direction along the surface, the minimum grid size is $1 \times 10^{-1} R_{C1}$ on the shoulder to resolve the flowfield there and is as large as 5 times this value in the nose region to reduce the computational time. These values of the grid sizes have been established to ensure grid independence of the solution at peak heating ($t = 54$ s) condition. Calculations were done using the CRAY C90 (Eagle) and the CRAY J90 (Newton) computers located at the NASA Ames Research Center. The computational time required is about 200 CPU and 600 CPU seconds per global pass for the nonequilibrium and equilibrium flow calculations around the body (without radiation), respectively, on the CRAY C90 computer. Typically, two global passes are required for convergence of the shock shape and surface heating.

Nonablating Results Along the Trajectory with Nonequilibrium and Equilibrium Chemistry

Nonablating stagnation-point total heat-transfer rate (conduction + diffusion + radiation) is provided at different times along the entry trajectory in Fig. 3. Results are obtained with equilibrium as well as nonequilibrium (finite-rate) flowfield chemistry. Three surface recombination boundary conditions, namely, full catalytic wall (FCW), equilibrium catalytic wall (ECW), and noncatalytic wall (NCW) are used with the finite-rate chemistry calculations. Present results for the fully catalytic wall (FCW) case are in good agreement with those obtained by Olynick, et al.² up to time $t = 60$ s. A maximum value of about 1250 W/cm^2 is obtained at $t = 54$ s from the present calculations. Corresponding value obtained from Ref. 2 is a bit higher. However, the difference between these two values increases for $t > 60$ s and may be due to grid resolution employed in Ref. 2. Further, the present finite-rate results with an equilibrium catalytic wall (ECW) boundary condition are close to the equilibrium flow results as expected. A maximum value of about 1100 W/cm^2 is obtained at $t = 54$ s in this case. The noncatalytic wall (NCW) predictions are included for reference and give the lowest surface heating with a maximum value of only about 650 W/cm^2 at $t = 54$ s.

The radiation component for total nonequilibrium heating is obtained from the corresponding equilibrium calculations and is about 115 W/cm^2 at peak heating ($t = 54$ s). Figure 4 shows the presently computed stagnation-point equilibrium radiative heat transfer rate as well as the values obtained in Ref. 2 from a nonequilibrium radiation calculation. It is not clear why the nonequilibrium radiative heating is lower at earlier times and higher at later times in the trajectory as compared to the equilibrium calculations. Generally, the nonequilibrium effects (which are likely to be present at earlier times in the trajectory) should increase²⁶ radiative heating in comparison to the equilibrium value and it should approach the equilibrium value at later times in the trajectory (with the increasing Reynolds number).

The radiative equilibrium wall temperatures for the heating calculations of Fig. 3 are shown in Fig. 5. A value of 0.9 is used for char emissivity (ϵ) in the present calculations. Similar to the surface heat transfer values, present fully catalytic wall predictions for surface temperature are in good agreement with those of Olynick, et al.². Reference 2 employed a value of 1.0 for ϵ , assuming zero reflectivity.

Figure 5 shows recomputed Olynick's values with $\epsilon = 0.9$. Differences between the present predictions and those of Ref. 2 increase at a later time in the trajectory for the reasons mentioned earlier. For most of the investigated trajectory, the surface temperatures are greater than 3000 K. Consequently, the fully catalytic wall (FCW) boundary condition is physically inappropriate since full recombination of air (for FCW boundary condition) cannot be forced for temperatures greater than about 2000 K. A physically appropriate surface recombination condition for these temperatures is a finite catalytic wall condition, which would be bounded by the ECW (most conservative) and the NCW boundary conditions. A maximum value of about 3800 K is obtained at $t = 54$ s for the present finite-rate results with an ECW wall condition. These results are close to those obtained with the equilibrium flowfield chemistry as expected. The noncatalytic wall (NCW) calculations give the lowest surface temperatures as noted with the surface heating results of Fig. 3.

Ablation Results Along the Trajectory with Equilibrium Chemistry

Figure 6(a) shows the equilibrium stagnation total heat transfer rate with and without ablation along the trajectory. Ablation produces a 35% reduction in the heating at peak heating time of $t = 54$ s. The corresponding peak stagnation heat transfer rate of Ref. 2 (without ablation) is about 10% higher than the present value, and their results also show a reduction of about 35% with ablation. Components of the total heat transfer rates of Fig. 6(a) are shown in Fig. 6(b). Reduction in the convective component, q_c (which is given by Eq. (8) and consists of conduction, diffusion, and convection) by ablation is due to injection cooling. Ablation injection reduces the surface gradients of temperature and that of various species mass fractions, causing a decrease in the conductive and diffusive heat fluxes. The radiative component, which is relatively small (less than 11% of the total heating without ablation), is not impacted much by ablation injection. There is a slight increase in radiation with ablation before the peak heating ($t = 54$ s). There is a deeper penetration of the shock layer by the ablation species C and CO during earlier times in the trajectory, and the increase in radiation from C line and CO(4+) molecular contributions is only partially offset by the absorption of radiation by ablation species during that period.

Surface temperatures used with the equilibrium stagnation heating calculations are given in Fig. 7. Surface heating without ablation is obtained by using the radiative equilibrium wall temperature as mentioned previously (see Fig. 5), whereas the ablation temperature from Eq. (3) is used for the ablation injection calculations. No ablation temperatures are generally higher (due to the higher surface heating) than those with ablation. Present ablation temperature values are close to those obtained by Olynick, et al. (Ref. 2) up to the peak heating time ($t < 54$ s) in the trajectory. At later times, present values are lower by a maximum of about 18% (at $t = 76$ s). Also shown in Fig. 7 is the mass fraction of ablation species at surface, with a maximum value of about 0.25 at peak heating time ($t = 54$ s). This implies that 75% of the mass at surface is from the freestream at that time in the trajectory.

The surface ablation injection rate along the trajectory as well as the ratio of injection rate to the freestream mass flux, corresponding to the heat transfer rate of Fig. 6(a), are shown in Fig. 8. A maximum value of 3% of the ratio is obtained at time $t = 34$ s. The value of this ratio decreases to about 1.5% at peak heating, where the maximum injection rate of about $0.04 \text{ kg/m}^2\text{-s}$ is obtained. Even though similar reduction (35%) in heating is obtained with ablation, presently computed values of the injection rate and injection mass flux ratio at peak heating ($t = 54$ s) are about one-half of those obtained in Ref. 2. It is believed that these differences are due to the differences in surface elemental composition, and, consequently, the fraction of ablation species, and their enthalpies used in the two calculations. Present quasi-steady ablation assumption would also contribute to these differences.

Laminar/Turbulent Ablation Results at Peak Heating Condition with Equilibrium Chemistry

Stagnation Profiles. Figure 9 shows the temperature and ablator mass-fraction profiles at peak heating ($t = 54$ s). The effect of ablation injection is limited to about 20% of the flowfield close to the surface at that time. This is also evident from the mass-fraction profiles of the freestream and ablation species shown in Fig. 10. The dominant ablation species not included in Ref. 2 are C_2H , C_3H , and C_4H . Non-inclusion of these species may be partly responsible for the differences in present mass loss rate and those of Ref. 2 as mentioned earlier (See Fig. 8).

Forebody Surface Distributions. Surface distributions of the total heat flux for laminar and fully turbulent flow cases over the forebody of the Stardust Capsule are given in Fig. 11. This figure shows the effect of both ablator (PICA) mass injection and turbulence on total heating distributions for the peak heating time of $t = 54$ s along the trajectory. The coupled PICA mass injection distributions are shown in Fig. 12. The impact of ablation injection on total heating is very pronounced for the laminar flow. In this case, the total heating is reduced by about 35% along the forebody (as compared to the nonablating surface), essentially through the reduction of the convective component as discussed earlier for the stagnation point. However, for the turbulent solutions, where the flow is assumed to undergo instantaneous transition at s/R_n equal to 0.05, the reduction in total heating is less than 13% as compared to the nonablating laminar flow value on both the conical flank and shoulder. Obviously the benefit of ablation injection in reducing the heating for the laminar flow is partially negated when the flow is assumed to be turbulent. The mass injection rate distributions of Fig. 12, in general, follow the surface heat flux distributions of Fig. 11. The stagnation nondimensional injection rate, $\dot{m}/\rho_\infty V_\infty$, of 0.015 corresponds to a dimensional value of about $0.040 \text{ kg/m}^2\text{-s}$ (as noted earlier also).

There is no noticeable effect of ablation injection and turbulence on surface pressure distribution as shown in Fig. 13. The stagnation ($s = 0$) pressure in this figure is about $28,000 \text{ N/m}^2$. This value as well as the pressure distribution are similar to those of Ref. 2.

Concluding Remarks

Results are presented for the forebody of the Stardust Sample Return Capsule entering the Earth's atmosphere. Solutions are obtained from an axisymmetric viscous shock-layer (VSL) analysis with and without surface ablation, including the effect of turbulence.

The forebody aeroshell consists of a 60-degree sphere cone with a shoulder radius one-twelfth that of the nose. For proper resolution of the flowfield over the shoulder, the VSL equations are scaled with the shoulder radius in place of the conventionally employed nose radius. These equations are globally iterated with the Vigneron pressure condition to treat

the large embedded subsonic region between the stagnation line and the supersonic outflow at the top of the shoulder.

The no ablation VSL calculations employ an 11-species nonequilibrium chemistry model. For these calculations, an equilibrium catalytic wall (ECW) boundary condition is physically consistent and appropriate to use in place of the fully catalytic wall (FCW) condition (with complete recombination to the freestream species). The fully coupled ablation injection calculations are done with a 20-species equilibrium chemistry model. With fully equilibrium calculations, the elemental conservation equations are solved (iteratively) for each element to determine the elemental composition at the surface (adjacent to the ablator) and in the flowfield. The solution of elemental conservation equations provide a unique solution to the boundary-value problem. Further, for the case when the ablation injection rate is small and the gas composition at the surface is due to both the freestream and ablation products, the species boundary condition problem at the surface encountered with finite-rate calculations is avoided. The small injection rates are usually encountered before large scale oxidation and sublimation drive the species due to the freestream away from the surface.

The maximum stagnation heating of about 1250 W/cm² is obtained without ablation injection with nonequilibrium calculations and complete surface recombination, (i.e., FCW boundary condition) whereas a value of about 1100 W/cm² is obtained for a more realistic equilibrium catalytic wall (ECW) boundary condition with a radiative equilibrium wall temperature of about 3800 K. Stagnation heating similar to the later value is obtained with a fully equilibrium calculation. The maximum value of radiative heating component is about 11% at peak heating. With ablation injection, a decrease of about 35% in the total stagnation-point heating (with equilibrium chemistry) is obtained at the peak-heating point in the trajectory. Reduction in heating is slightly less downstream of the stagnation point and along the conical flank, including the shoulder for the laminar case. For the turbulent solutions where the flow is assumed to undergo instantaneous transition just downstream of the stagnation line, the heating is reduced by only about 13% on the conical flank and shoulder as compared to the nonablating laminar flow. Augmentation of the convective heating by turbulence appears to partially negate the

benefit of heating reduction due to ablation injection in this case.

Acknowledgments

The author would like to gratefully acknowledge the following contributions: Dr. K. Sutton obtained the curve fits for ablation temperature used in this work; Dr. J. N. Moss helped with the discussion concerning the specification of species boundary condition with small injection rates; and Dr. R. A. Mitcheltree provided helpful suggestions during the preparation of this manuscript.

References

1. Atkins, K.L., Brownlee, D.E., Duxbury, T., Yen, C., and Tsou, P., "STARDUST: Discovery's Interstellar Dust and Cometary Sample Return Mission," Proceedings from the 1997 IEEE Aerospace Conference, Feb. 1997.
2. Olynick, D., Chen, Y.-K., and Tauber, M., "Forebody TPS Sizing with Radiation and Ablation for the Stardust Sample Return Capsule," AIAA Paper 97-2474, June 1997.
3. Gupta, R.N., Lee, K.P., and Scott, C.D., "Aerothermal Study of Mars Pathfinder Aeroshell," *Journal of Spacecraft and Rockets*, Vol. 33, No. 1, Jan.-Feb. 1996, pp. 61-69.
4. Park, C. and Ahn, H.K., "Stagnation-Point Heat Transfer Rates for Pioneer-Venus Probes," AIAA Paper 98-0832, Jan. 1998.
5. Wakefield, R.M. and Pitts, W.C., "Analysis of the Heat-Shield Experiment on the Pioneer-Venus Entry Probes," AIAA Paper 80-1494, July 1980.
6. Ahn, H.K. and Park, C., "Preliminary Study of the MUSES-C Reentry," AIAA Paper, Jan. 1997.
7. Ahn, H.K., Park, C., and Sawada, K., "Dynamics of Pyrolysis Gas in Charring Materials Ablation," AIAA Paper 98-0165, Jan. 1998.
8. Suzuki, K., Kubota, H., Fujita, K., and Abe, T., "Chemical Nonequilibrium Ablation Analysis of MUSES-C Super-orbital Reentry Capsule," AIAA Paper 97-2481, June 1997.
9. Gupta, R.N., Lee, K.P., and Zoby, E.V., "Enhancements to Viscous-Shock-Layer Technique," *Journal of Spacecraft and Rockets*, Vol. 30, No. 4, July-August 1993, pp. 404-413.
10. Gupta, R.N., Lee K.P., Moss, J.N., and Sutton, K., "Viscous Shock-Layer Solutions with Coupled Radiation and Ablation for Earth Entry," *Journal of Spacecraft and Rockets*, Vol. 29, No. 2, March-April 1992, pp. 173-181.
11. Moss, J.N., Simmonds, A.L., and Anderson, E.C., "Turbulent Radiating Shock Layers with

- Coupled Ablation Injection," *Journal of Spacecraft and Rockets*, Vol. 17, No. 3, May-June 1980, pp. 177-183.
12. Gupta, R.N., Yos, J.M., Thompson, R.A., and Lee, K.P., "A Review of Reaction Rates and Thermodynamic and Transport Properties for an 11-Species Air Model for Chemical and Thermal Nonequilibrium Calculations to 30,000 K," NASA RP 1232, Aug. 1990.
 13. Gupta, R.N., Moss, J.N., Zoby, E.V., and Simmonds, A.L., "An Evaluation of Turbulence Models for Massively Blown Surfaces," *Entry Vehicle Heating and Thermal Protection Systems: AIAA Progress in Astronautics and Aeronautics*, Vol. 85, edited by P.E. Bauer and H.E. Collicott, AIAA New York, 1983, pp. 446-471.
 14. Gupta, R.N., Lee, K.P., Zoby, E.V., Moss, J.N., and Thompson, R.A., "Hypersonic Viscous Shock-layer Solutions over Long Slender Bodies—Part I: High Reynolds Number Flows," *Journal of Spacecraft and Rockets*, Vol. 27, No. 2, March-April 1990, pp. 175-184.
 15. Stroud, C.W. and Brinkley, K.L., "Chemical Equilibrium of Ablation Materials Including Condensed Species," NASA TN D-5391, 1969.
 16. Tran, H., Johnson, C., Rasky, D., Hui, F., Chen, Y.K., and Hsu, M., "Phenolic Impregnated Carbon Ablators (PICA) for Discovery Class Mission," AIAA 96-1911, June 1996.
 17. Bartlett, E.P. and Kendall, R.M., "An Analysis of the Coupled Chemically Reacting Boundary Layer and Charring Ablator," Pt. 3, NASA CR-1062, June 1968.
 18. Anon., "Aerotherm Charring Material Thermal Response and Ablation Program (CMA 87S)," Acurex, Rept. UM-87-13/ATD, Mountain View, CA, Nov. 1987.
 19. Nicolet, W.E., "Advanced Methods for Calculating Radiation Transport in Ablation Product Contaminated Boundary Layers," NASA CR-1656, Sept. 1970.
 20. Nicolet, W.E., "User's Manual for the Generalized Radiation Transfer Code (RAD/EQUIL)," NACA CR-116353, Oct. 1969.
 21. Shinn, J.L., "Optical Absorption of Carbon and Hydrogen Species from Shock Heated Acetylene and Methane in the 135-220 m Wavelength Range," *Thermophysics of Atmospheric Entry*, edited by T.E. Horton, Vol. 82, *Progress in Astronautics and Aeronautics*, AIAA, New York, 1982, pp. 68-80.
 22. Armaly, B.F. and Sutton, K., "Viscosity of Multicomponent Partially Ionized Gas Mixtures," AIAA Paper 80-1495, July 1980.
 23. Mason, E.A., and Saxena, S.C., "Approximation Formula for the Thermal Conductivity of Gas Mixtures," *Physics of Fluids*, Vol. 1, No. 5, pp. 361-369.
 24. Cebeci, T. and Smith, A.M.O., *Analysis of Turbulent Boundary Layers*, Academic Press, New York, 1974.
 25. Gupta, R.N., "Turbulence Modeling of Flowfields with Massive Surface Ablation," *Journal of Spacecraft and Rockets*, Vol. 20, No. 6, Nov.-Dec. 1983, pp. 531-538.
 26. Park, C., "Radiation Enhancement by Nonequilibrium in Earth's Atmosphere," AIAA Paper 83-0410, Jan. 1988.

Table 1 Coefficients for ablation temperature for PICA

Coefficients	$j = 1$	2	3	4	5
α_{1j}	3790.0	86.795	-2980.0	-8250.2	-7631.7
α_{2j}	329.94	-66.703	-1524.6	-4340.9	-3885.7
α_{3j}	20.386	-17.654	-268.62	-771.00	-684.89

Table 2 Freestream conditions for Stardust entry trajectory

Time, s	Altitude, km	Velocity, m/s	Density, kg/m ³	Temperature K
34.00	81.64	12,590.4	9.63×10^{-6}	216.93
42.00	71.92	12,413.4	1.29×10^{-5}	221.42
48.00	65.44	12,004.0	1.06×10^{-4}	229.00
54.00	59.77	11,136.7	2.34×10^{-4}	238.47
60.00	55.02	9,718.7	4.39×10^{-4}	248.48
66.00	51.19	7,956.9	7.21×10^{-4}	253.55
76.00	46.51	5,178.9	1.35×10^{-3}	256.90

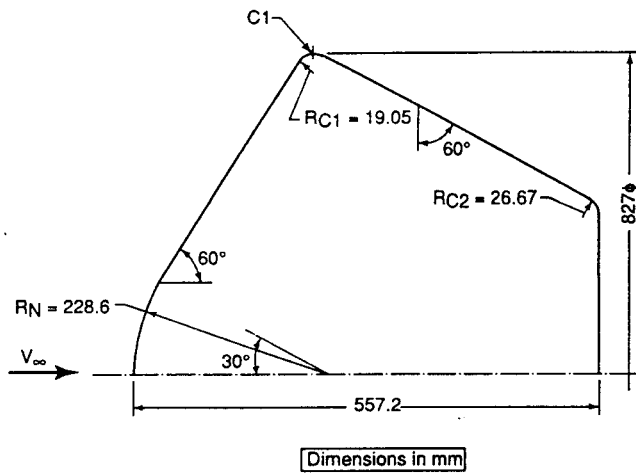


Fig. 1 Geometry of stardust sample return capsule.

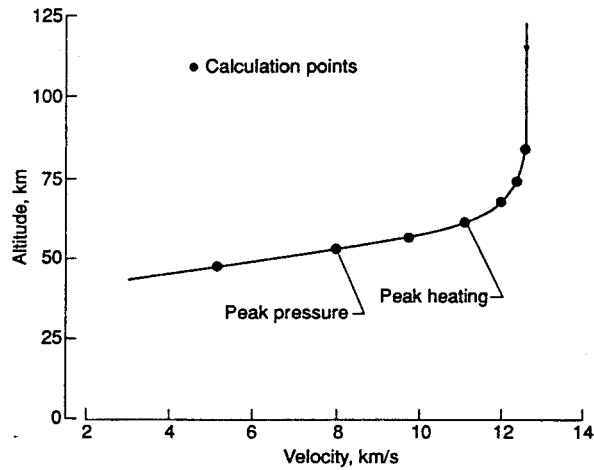


Fig. 2 Stardust entry trajectory.

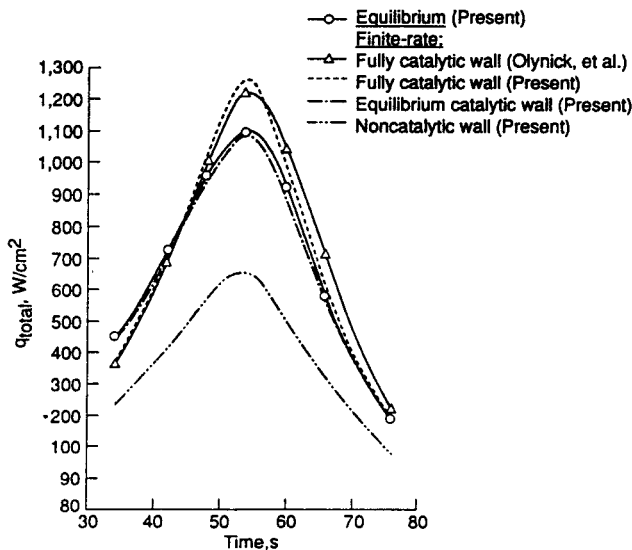


Fig. 3 Nonablating stagnation-point total heat transfer rate.

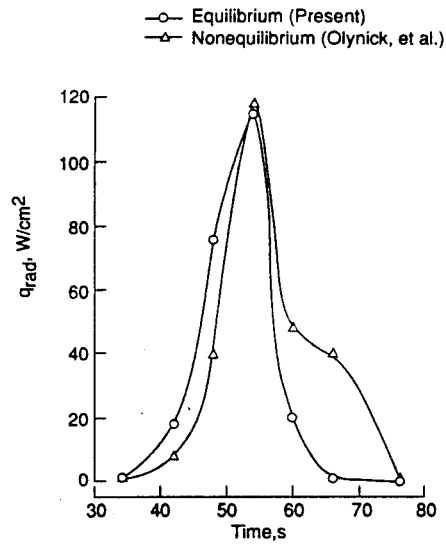


Fig. 4 Nonablating stagnation-point radiative heat transfer rate.

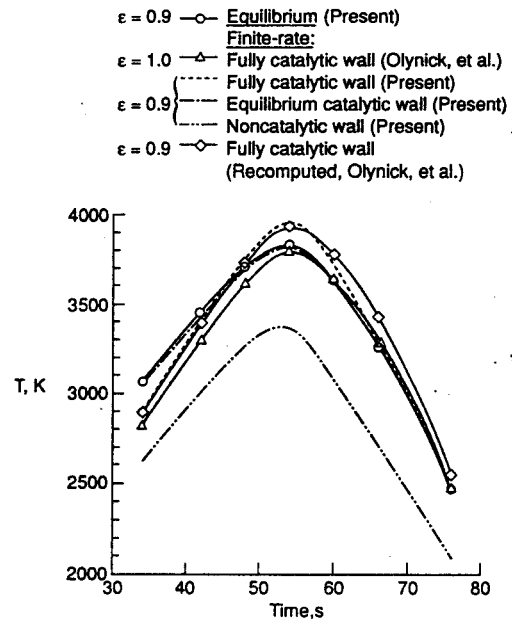


Fig. 5 Nonablating stagnation-point temperature.

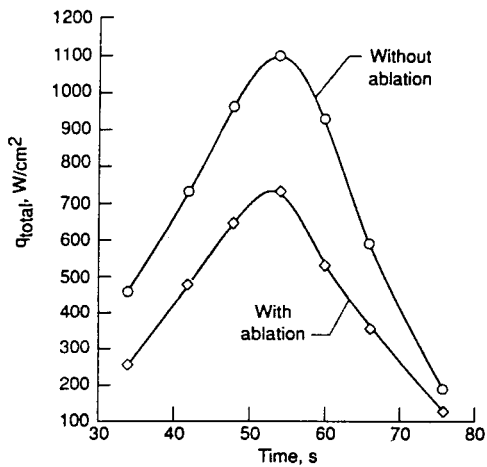


Fig. 6 (a) Equilibrium stagnation-point total heat transfer rate.

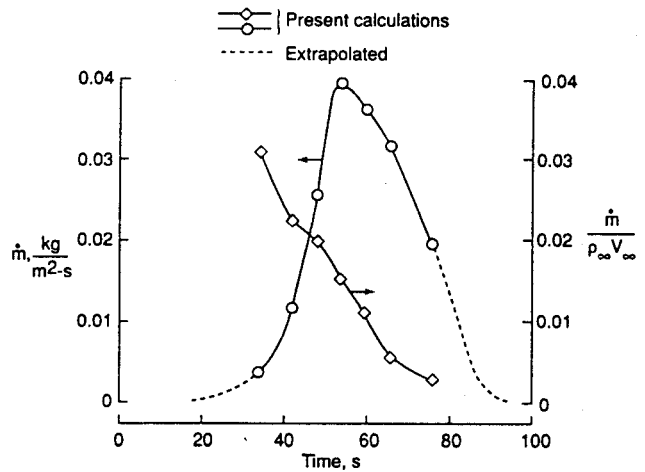


Fig. 8 Equilibrium stagnation-point mass injection rate.

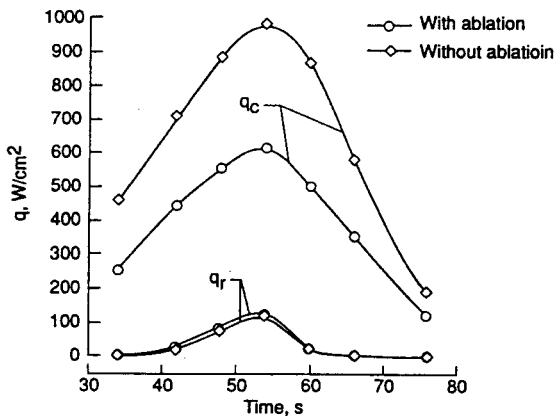


Fig. 6 (b) Components of equilibrium stagnation-point heat transfer rate.

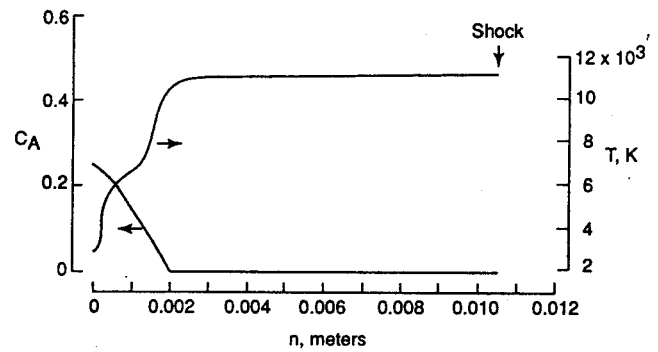


Fig. 9 Stagnation ablator mass-fraction & temperature profiles [equilibrium flow; peak heating ($t = 54s$)].

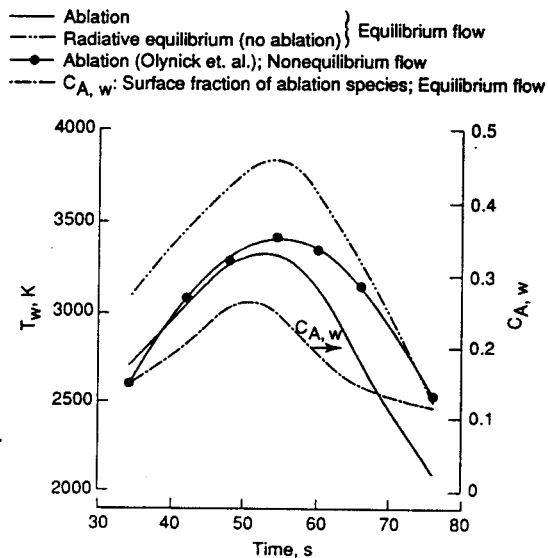


Fig. 7 Stagnation-point surface temperature and ablation mass-fraction.

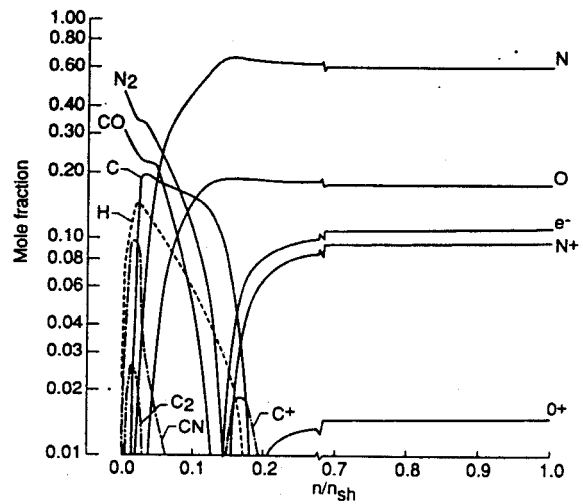


Fig. 10 (a) Stagnation freestream and ablation species profiles [equilibrium flow; peak heating ($t = 54s$), $n_{sh} = 0.0105m$].

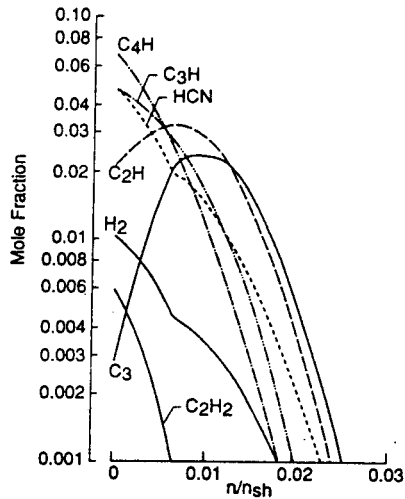


Fig. 10 (b) Stagnation ablation species profiles [equilibrium flow; peak heating ($t = 54s$), $n_{sh} = 0.0105m$].

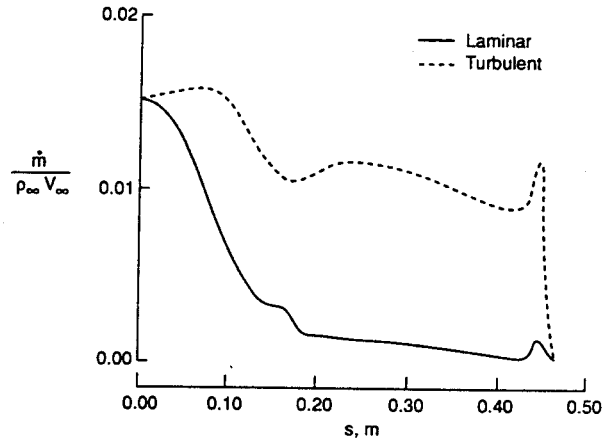


Fig. 12 Mass injection rate distribution [equilibrium flow; peak heating ($t = 54s$)].

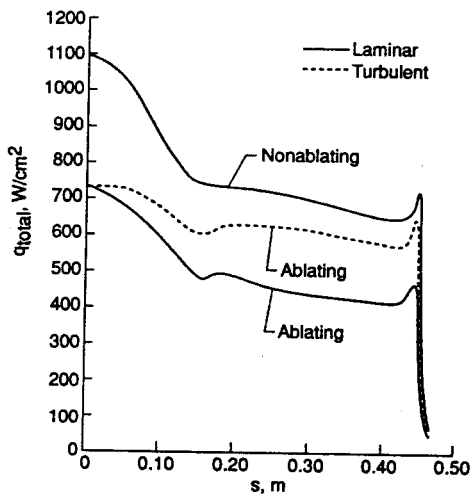


Fig. 11 Total surface heat flux distribution [equilibrium flow; peak heating ($t = 54s$)].

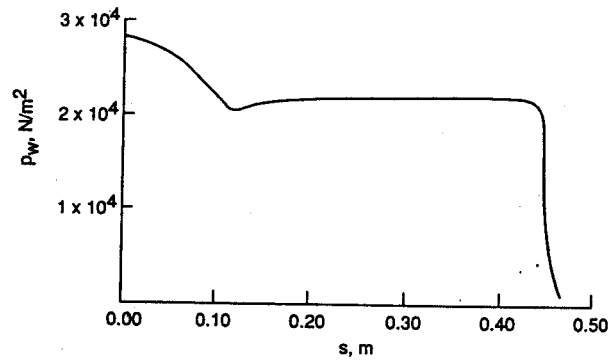


Fig. 13 Surface pressure distribution (nonablating/ablating) [equilibrium flow (laminar/turbulent); peak heating ($t = 54s$)].